

AN ABSTRACT OF THE THESIS OF

Tyler Law for the degree of Master of Science in Nuclear Engineering presented on March 28, 2023.

Title: Benchmark Comparison of the Oregon State TRIGA® Reactor Between MCNP6 and Serpent 2.

Abstract approved: _____

Steven Reese

A model of the Oregon State TRIGA® reactor was developed in Serpent 2 by translating a previously accepted MCNP model. Both models were verified and validated via comparison of each model and data gathered from the core start-up. Reactivity bias in each code was determined. Using the rod drop method, the rod worth of the four control rods measured was compared to model predictions. Additionally, shutdown margin and core excess were calculated. Both models were applied to solve for the average neutron lifetime and delayed neutron fraction values. Further V&V includes side-by-side comparisons of power-per-element and the temperature coefficient of reactivity. The Serpent 2 model was determined to be equivalent to the previously accepted MCNP model as well as the reactor physics.

©Copyright by Tyler Law
March 28, 2023
All Rights Reserved

Benchmark Comparison of the Oregon State TRIGA® Reactor Between MCNP6 and Serpent 2.

by
Tyler Law

A THESIS

submitted to

Oregon State University

in partial fulfillment of
the requirements for the
degree of

Master of Science

Presented March 28, 2023
Commencement June 2023

Master of Science thesis of Tyler Law presented on March 28, 2023

APPROVED:

Major Professor, representing Nuclear Engineering

Head of the School of Nuclear Science and Engineering

Dean of the Graduate School

I understand that my thesis will become part of the permanent collection of Oregon State University libraries. My signature below authorizes release of my thesis to any reader upon request.

Tyler Law, Author

ACKNOWLEDGEMENTS

I would like to thank Dr. Reese. His endless patience and support have kept me going through everything. The near endless experience and wealth of knowledge are something I admire and will strive for in my future.

To my wife, Emily, thank you for being with me through this selfish journey. You have spent years letting me explore, while you worked hard to keep us on sure footing. I don't know how to express just how much you have made my life better, but I will try. Even if it takes me a lifetime.

To Tucker, my one year old son. You took me through a wild ride, but it was all worth it. Watching you discover the world with brand new eyes has been an inspiration. It is crazy just how much of a difference one year makes, and I am excited to see you grow.

TABLE OF CONTENTS

	<u>Page</u>
1.0 Introduction	1
2.0 Objective	3
3.0 Literature Review	4
3.1 MCNP	4
3.2 OSTR and MCNP	7
3.3 Molybdenum Feasibility	10
3.4 SERPENT	10
3.5 Delta-Tracking	12
3.5 Dynamic capability	13
3.6 Comparison of tools	13
3.7 Homogenization of reactors	15
4.0 Materials and Methods	17
4.1 Oregon State TRIGA® Reactor	17
4.2 Nuclear Reaction Data Library	22
4.3 Critical Rod Configurations	22
4.4 Critical Bias	25
4.5 Point-Kinetic Parameters	26
4.6 Experimental Point-Kinetic Parameters	27
4.6.1 Neutron Lifetime	27
4.6.2 Effective Delayed Neutron Fraction	28

TABLE OF CONTENTS (Continued)

	<u>Page</u>
4.7 MCNP Point-Kinetic Calculations	29
4.7.1 Neutron lifetime	29
4.7.2 Effective Delayed Neutron Fraction	31
4.8 Serpent 2 Point-Kinetic Calculations	32
4.8.1 Nauchi Neutron Lifetime	32
4.8.2 Nauchi Delayed Neutron Fraction	33
4.8.3 Iterated Fission Probability Neutron Lifetime	33
4.8.4 Iterated Fission Probability Delayed Neutron Fraction	34
4.8.5 Perturbation Neutron Lifetime	35
4.8.6 Perturbation Neutron Fraction	36
4.9 Experimental Rod Worth Calibration	36
4.10 MCNP/Serpent Rod Worth Calculation	37
4.11 Shutdown Margin and Core Excess	39
4.12 Power Per Element	39
4.13 Temperature Coefficient of Reactivity	40
5.0 Results	41
5.1 MCNP and SERPENT 2 Bias	41
5.2 Point-Kinetic Parameters	42
5.3 Rod Worth	43
5.4 Core Excess and Shutdown Margin	45

TABLE OF CONTENTS (Continued)

	<u>Page</u>
5.5 Power Per Element	46
5.5.1 Side by Side Comparison	46
5.5.2 Mean and Maximum Difference	48
5.6 Temperature Coefficient of Reactivity	49
6.0 Discussion	50
7.0 Conclusion	52
8.0 Future Work	53
9.0 References	54
10.0 Appendix	58

LIST OF FIGURES

	<u>Page</u>
Figure 1: OSTR Horizontal Cross Section (Oregon State University, 2018)	17
Figure 2: OSTR Vertical Cross Section (Oregon State University, 2018)	18
Figure 3: CLICIT core configuration (Oregon State University, 2018)	19
Figure 4: Instrumented Fuel Element (Oregon State University, 2018)	20
Figure 5: Fuel Element and Control Rod Layout (Oregon State University, 2018)	21
Figure 6: Total rod worth compared to core excess and shutdown margin (Oregon State University, 2018)	39
Figure 7: Transient rod worth vs percent withdrawn	44
Figure 8: Safe rod vs percent withdrawn	45
Figure 9: Reg rod vs percent withdrawn	45
Figure 10: Shim rod vs percent withdrawn	46
Figure 11: MCNP power per element for trial 3	48
Figure 12: Serpent 2 power per element for trial 3	48
Figure 13: Maximum power difference per element between MCNP and Serpent	49
Figure 14: Average power difference per element between MCNP and Serpent	50
Figure 15: Reactivity vs Temperature.	51

LIST OF TABLES

	<u>Page</u>
Table 1: Critical control rod configurations	24
Table 2: Delayed neutron fraction and decay constants	27
Table 3: Control rod calibration configurations	38
Table 4: Critical Bias Trial Results	41
Table 5: Point-Kinetic Parameter results	43
Table 6: Core excess and shutdown margin results.	45
Table 7: Core excess and shutdown margin as compared to the total rod worth	46
Table 8: Reactivity at different temperatures	50

LIST OF APPENDICES

	<u>Page</u>
Appendix A	58
Appendix B	59
Appendix C	62

1.0 Introduction

Licensing and operating a nuclear reactor requires extensive verification that it can run safely. The Nuclear Regulatory Commission legislates through the Code of Federal Regulations (10 CFR) standards of safety which must be met in order to operate. These safety standards can be verified through small scale experiments, and first principle physics modeling. Understanding how a reactor may function allows for better control and can prevent negative outcomes such as facility damage, accidental radiation exposure, and damage to life and the environment. This is complicated by complex reactor designs and diverse material interactions.

Several software packages have been developed to model the physics of a reactor for this purpose. Broadly speaking, these programs can be grouped into two categories: deterministic and stochastic. Deterministic codes solve physics-based equations directly using algebraic methods. Stochastic codes use Monte Carlo methods to solve the same equations. They do this by running multiple simulations to determine probabilistic outcomes. This thesis compares two stochastic codes, Monte-Carlo n-particle (MCNP) (X-5, 2008) and Serpent 2 (Leppänen, 2015), and their ability to model the transport of neutrons for the Oregon State Mark II Teaching, Research, and Isotope General Atomics (TRIGA[®]) reactor.

The Oregon State TRIGA[®] reactor (OSTR) is a research reactor designed to be exceptionally safe. The OSTR includes safety systems that do not require operator input such as electric driven control rods that release during a loss of power event, and the application of materials which reduce the reactivity as temperature increases.

The reactor has two modes of operation: steady-state, and transient. During steady state operation, the rate of change in the power is regulated by the control rods. The rods absorb enough prompt neutrons to allow the delayed neutrons to control the neutron population. This allows for both greater control of the reactor and longer run times. A pulse rapidly withdraws the transient control rod from the system, creating a large change in the neutron population driven largely by prompt neutrons. Following the transient, the reactor is immediately shut down because the rate of growth is too fast to control.

There are several experimental facilities which are used to bombard an experiment with neutrons. To use any of these facilities, the proposed experiment must be shown to meet the standards set within the technical specifications of the reactor. This can be done by simulating the experiment in MCNP, which has been shown to be a valid tool for modeling the OSTR when comparing it to experiments performed during the initial reactor startup.

Kitto (2012), Hartman et al. (2013), and several others have shown and verified the OSTR's MCNP model accurately represents the steady-state physics of the reactor. They did this by comparing MCNP's solution of several key characteristics of the reactor to physical experiments.

The most significant problem is that MCNP was designed only for steady-state operation. The first launch of MCNP was in 1977 (Sood, 2017). For technology at that time, steady-state calculations were computationally expensive. Updates were largely particle interaction

improvements (Sood, 2017), but never included any form of transient support. Serpent, however, was built with transient capabilities. Currently there is no validated Serpent OSTR model. The purpose of this work is to compare MCNP and Serpent 2 using the same key characteristic used to validate the use of MCNP.

2.0 Objective

The overall objective of this work is to determine if the Serpent 2 model is capable of and as accurate as MCNP at modeling steady-state physics for the OSTR. Note that ‘steady-state’ is different in this context than the OSTR’s modes of operation. This assumes there are no changes in geometry or material, and the rate of neutron production is held constant. This is the first step of validation, since steady-state reduces the variables to just material and geometry. Through this work, further validation of the transient capabilities of the Serpent 2 model can be performed.

Eight characteristics were considered, including: critical bias, delayed neutron fraction, prompt neutron lifetime, control rod worth, core excess, shutdown margin, power per element, and temperature coefficient. If Serpent 2 results were found to be similar to MCNP in predicting real-world physics, then the model would be considered valid.

3.0 Literature Review

3.1 MCNP

The Monte-Carlo n-particle (MCNP) is a software package that assesses the movement and interactions of neutrons, photons, and electrons. It does this through stochastic methods, meaning that instead of solving the transport equation directly for the particle behavior, the program will use pseudo-random samples to determine the probable outcomes. The software package does this by tracking, "each of many particles from a source throughout its life to its death" (X-5, 2008) be it from absorption, escape, or another mechanism. Important events are tallied, such as absorptions, movement from one cell mesh into another, etc. From this information such as flux or the neutron multiplication rate can be generated.

The program's algorithm allows it to solve problems considering complicated geometry which may prove difficult to solve deterministically. Using simple surfaces, the software defines areas with specific material properties. Using this method, it is possible to build a virtual reactor with various boundary conditions (i.e., vacuum, reflective, or albedo). All materials have some probability of interaction. This includes the scattering, absorption, and fission cross-sections, σ , as well as, an average number of particles per fission event (ν) and the energy distribution (X) of said particles. Additionally, it takes in the thermal scattering ($S(\alpha,\beta)$) data libraries which dictate the elastic and inelastic scattering of a particle, described more below.

When all the data is defined, MCNP begins sampling particles by choosing a pseudo-random direction and determining a distance to travel in that direction until it either

collides with a defined material or passes through a boundary. The path length is determined by Eq. 1 where ξ is a uniform random number. If there is a collision, there are three outcomes. The first, the particle scatters, and there is a new energy and direction associated with it. Second, the particle may be absorbed leading to an emission. Finally, the particle could collide with an atom causing fission. A particle which passes through a boundary has a few different outcomes. Either it can exit the system through a vacuum boundary condition and is then considered lost to the system, it can be stopped at the boundary and the direction it travels is reversed in a reflective boundary, or there can be some ratio of between boundary conditions. The particle is tracked until it is either absorbed, fissions, or is lost.

$$l = \frac{-\log \xi}{\Sigma_{tot}}$$

Eq. 1

In most cases, calculation of the overall neutron multiplication for a model reactor, also known as the effective k-eigenvalue (k_{eff}), is necessary. Monte Carlo n-particle does this by taking the time-integrated Boltzmann equation (Eq 2) and reducing it to Eq 3 (X-5, 2008). In both equations, ρ_a is the atomic density, and V is a volume in the form of radius over some angle. E and Ω are energy and angle, J is a net current crossing a boundary, and ϕ is the particle flux. The probability of transport are given as σ_t and σ_s representing a total cross section and scatter cross section respectively. The last two are σ_f and ν which represent the probability of fission over some distance in terms of a microscopic cross section and the average number of particles born from fission.

$$\begin{aligned}
& \int_V \int_0^\infty \int_E \int_\Omega \nabla \cdot J dV dt dE d\Omega + \rho_a \int_V \int_0^\infty \int_E \int_\Omega \sigma_t \Phi dV dt dE d\Omega \\
&= \frac{1}{k_{eff}} \rho_a \int_V \int_0^\infty \int_E \int_\Omega v \sigma_f dV dt dE d\Omega + \rho_a \int_V \int_0^\infty \int_E \int_\Omega \sigma_s' \Phi' dV dt dE d\Omega
\end{aligned}$$

Eq 2

$$k_{eff} = \frac{\text{fission neutrons}_{n+1}}{\text{fission neutrons}_n} = \frac{\rho_a \int_V \int_0^\infty \int_E \int_\Omega v \sigma_f dV dt dE d\Omega}{\int_V \int_0^\infty \int_E \int_\Omega \nabla \cdot J dV dt dE d\Omega + \rho_a \int_V \int_0^\infty \int_E \int_\Omega \sigma_t \Phi dV dt dE d\Omega}$$

Eq 3

For k_{eff} , the numerator represents the new generation of neutrons caused by fission where the denominator is the total number of neutrons from the current generation. If k_{eff} is one, the system is critical. It is considered subcritical if k_{eff} less than one and supercritical if greater than one.

The program works by estimating starting conditions including, k_{eff} and neutron birth locations. Usually, k_{eff} is estimated as a value of 1 and homogeneous, unless defined otherwise. Over several generations, the algorithm converges on a k_{eff} , and neutron sources become more consistent. Monte Carlo n-particle lets a user-defined number of runs occur before starting to collect statistics, as the first few runs may not be accurate enough to count.

3.2 OSTR and MCNP

The first generation MCNP model of the OSTR core was written in 1997 strictly to characterize the epithermal flux from the reactor to the Neutron Radiography Facility (Schickler, 2013). The model was modified in 2005 during an effort to compute the flux characteristics in the inner core irradiation tube (ICIT), cadmium lined inner core irradiation tube (CLICIT), the Rotating Rack, and the Thermal Column (TC) although significant errors were found present. The model was updated in 2007, but the OSTR underwent conversion from high enriched uranium (HEU) to low enriched uranium (LEU) fuel in 2008.

In 2012, effort was made to verify the MCNP model using the core parameters throughout the HEU fuel's lifetime (Hartman, 2013). The baseline model was then used to compare the initial data from the LEU core. This data characterized the model bias, core excess, shutdown margin, fuel burnup, prompt neutron lifetime, delayed neutron fraction, temperature coefficient on reactivity, and power distribution within fuel rods. With the exceptions of the core excess and shutdown margin, all of the model data was in agreement with the experimental data.

Schickler (2013) used an updated MCNP model of the OSTR to compare energy-dependent neutron flux in the new LEU core with the old HEU fuel. He performed foil activation experiments and adjusted the MCNP output with experimental activities using a spectrum unfolding program called STAY'SL. Each of the foils maintain different neutron energy activation regions to allow for multiple energy sampling regions. The activation energies are based on ENDF/B-VII.0 cross-section plots and were used to determine the energy-dependent flux in various test facilities. Nickel, indium, and titanium were specifically used for threshold

reactions that occur only for fast-spectrum particles. For radiative capture reactions the materials, aluminum-gold, iron, scandium, lutetium-aluminum, tungsten, sodium chloride, and molybdenum were used.

Three of each foil type was used in each test facility at a variety of times. After irradiation, the samples were tested using an HPGe detector. The flux of each energy region was calculated using Eq 4 (Schickler., 2013) where C is the counts from a spectrum peak, λ is the decay constant, N_a is Avogadro's number, f_{iso} is the isotopic abundance of the nuclide, M is the atomic mass, f_γ is a branching fraction, Ω is a geometric efficiency of the detector, ϵ is the intrinsic efficiency of the detector, m is the mass of the sample, σ is a cross-section, t_0 is the irradiation time, and t_1 and t_2 are the start and end times respectively. There was little difference in the shape of the neutron flux versus energy curves between the HEU and LEU, and the experimental data was found to adequately match the MCNP model.

$$\Phi = \frac{C\lambda M \exp(\lambda t)}{f_\gamma f_{iso} \Omega_\epsilon m \sigma (1 - \exp(-\lambda t_0))(1 - \exp(-\lambda[t_2 - t_1]))}$$

Eq 4

Kitto updated the existing MCNP model in 2012 and determined the reactivity bias, which was previously lacking. The model was altered to include two additional beam ports, water saturation in graphite, manufacturer-specified fuel measurements, measured fuel impurities, and a hafnium impurity. The previous model only included two of the four beam

ports and assumed pure graphite. Also, the prior fuel was a generic blend of materials not consistent with the manufacturer. This verification was done to make a more accurate model to compare to the real world, including a suspected leak from the aluminum protecting the graphite from water (Kitto, 2012).

Updating the beam ports and swapping out the fuel is fairly straightforward as they are known and well-measured. The graphite is suspected to be saturated with water, but it was unknown to what extent (Kitto, 2012). Based on the theoretical density of 2.25 g/cm^3 and the as-built density of 1.698 g/cm^3 , an assumption of 30% saturation was estimated. The graphite saturation in the model was tested by increasing the water saturation by 5 atom percent to determine the change in reactivity. To test the Hafnium impurity in the fuel, Kitto tested different weight percentages from 5 to 10 in increments of 0.5%.

Kitto also analyzed the core loading configuration, adding specific fuel rods into the innermost rings to determine when it hits critical. Bias testing was executed by filling the core with the control rods and fuel. The control rods were lifted to determine various states where it became critical. This could be compared to the MCNP model and a bias determined. Kitto also analyzed the model's ability to determine each control rod's worth by individually withdrawing them in the software.

The overall sampling showed a change of + \$0.207 in reactivity when considering the differences between the old and new MCNP models (Kitto, 2012). Hafnium produced a negligible effect, meanwhile the beam port, water saturation, and fuel changes led to -\$0.164,

-\$0.454, and +\$0.894 respectively. An updated data library compensated for the rest.

Furthermore, the new MCNP model exhibited a \$0.273 bias, and the integrated rod-worth curves were slightly below the experimental results.

3.3 Molybdenum Feasibility

Over the last few years, there has been discussion about changing the core configuration to allow for production of Molybdenum-99 (^{99}Mo). The intent of this would be to fulfill the medical diagnostic needs of Technetium-99m, the radioactive progeny of ^{99}Mo .

There have been at least two studies to determine the feasibility of producing ^{99}Mo . In 1999, Seung-Hyuk Baik developed his own MCNP model of the OSTR to characterize the fission rate and power-per-element of fuel used specifically for Mo^{99} production. This was done before the fuel conversion and in 2012. A similar study was performed by Hummel (2013) using annular UO_2 fuel to accommodate for the low enrichment environment. Together, these studies were both able to show the viability and safety of converting part of the OSTR into a facility that produced medical isotopes.

3.4 SERPENT

Serpent is a monte carlo code used for lattice physics applications. Before it was developed, most codes tallied every occurrence, which resulted in an increased running time on

already prohibitively long calculations. The original code called, Probabilistic Scattering Game (PSG), was developed by VTT Technical Research Centre (Leppänen et al, 2015).

The focus of the original code was on generating homogenized group constants and simulating neutron transport in reactor geometries. The code relies on a Woodcock-based tracking routine, as opposed to surface-to-surface ray tracing used by MCNP, and a unionized energy grid for all cross-sections.

Serpent 1 is a revision of the PSG code which fixed several problems with the interaction physics. This included a burnup calculation routine and the Chebyshev Rational Approximation Method to solve the Bateman depletion equations (Leppänen, 2015). Overall, the code was suitable for 2-dimensional lattice physics and burnup calculations. Three-dimensional geometries required excessive memory usage that proved too limiting.

Serpent 2 is the most current version of the code. This revision was developed to deal with memory issues, previously mentioned. The most significant difference is that the unionized energy grid is optional, which changes how the cross-sectional data is handled. Also, additional methods of parallel calculation increased the number of calculations performed without additional memory usage.

3.5 Delta-Tracking

The most significant difference between MCNP code and Serpent k-eigenvalue calculation is the delta-tracking method developed by Woodcock, et al. Monte-Carlo n-Particle tracks particles as a piecewise function, whereas Serpent is a rejection sampling algorithm. Serpent uses the maximum cross-section from all the materials (Leppänen, 2017). The neutron is then traced using that cross-section to a virtual collision, using Eq 1, disregarding any borders it may cross. After a location is determined, the algorithm then determines if a true collision has occurred by comparing a pseudo-random number to the ratio of the true cross-section, Σ_{tot} , to the maximum cross-section, Σ_{maj} , (Eq 5). If the pseudo-random number is less than or equal to the fraction, a collision occurred (Leppänen, 2017).

$$P = \frac{\Sigma_{tot}(r,E)}{\Sigma_{maj}(E)}$$

Eq 5

This method can increase efficiency, but introduces drawbacks. For instance, a very localized material with a cross-section much larger than its surrounding material would not quickly converge (Leppänen, 2017). Also, delta tracking cannot use the track-length flux estimator because neutron paths may skip material regions and discontinuity points are not known (Leppänen, 2010).

3.5 Dynamic capability

In addition to the steady state calculations, Serpent has time-dependent tools. It simulates time dependent transport in two steps. It starts by calculating a precursor distribution of neutrons for steady-state conditions. Serpent then records this distribution and loads the new model with changes to the geometry, such as a dropped control rod. The second calculation follows the neutrons during the changes over small time intervals solving the time-dependent transport equation, Eq 6 (Leppänen, 2013).

$$\frac{1}{v} \frac{\delta}{\delta t} \Phi + \hat{\Omega} \cdot \nabla \Phi + \sum_{tot} \Phi = S + F + G$$

Eq 6

In this equation, simplified from Eq 2, S is the scatter source, F is the fission source, and G is an external source. Serpent allows for the manipulation of time steps and, based on Leppänen's initial tests, appears to converge on a curve with smaller time steps.

3.6 Comparison of tools

Castagna et al. (2018) developed a Serpent 1 model of the TRIGA® Mark II reactor in Pavia, similarly based on their own MCNP model. In comparison to the OSTR, the reactor in Pavia only differs in irradiation facilities and the cluster array geometry. The OSTR has two additional beam ports, as well as the ICIT and CLICIT, and a safety rod.

Several tests were performed to determine the accuracy of their current Serpent model. The benchmarking began with an analysis of a low-power critical reactor. In 26 different configurations, determined experimentally, they found the average bias of the model to be \$0.26 with a deviation of \$0.10 (Castagna, 2018). Secondly, a rod calibration was executed by taking a critical configuration, where a single control rod was down. Then the rod was gradually raised over several trials. The worth of each rod was determined to be within 10% accuracy of the experimental worth. Lastly, a direct comparison to MCNP using the same libraries, JEFF 3.1 was performed. This showed that Serpent was consistently \$0.06 above the MCNP bias.

This work suggests that there should be little difference between MCNP and Serpent. The conversion of the MCNP model to Serpent 2 should be similar for the OSTR. The only difference will be that we are using Serpent 2.1.31. While they did not specify a version, Serpent 1 can use continuous libraries, whereas version 2.1.31 can only use discrete libraries. The latest version, Serpent 2.1.32, allows for use of continuous libraries, but is not currently available due to software exports.

Future work with the OSTR serpent code could be used to perform transient simulations similar to the rod drop in the VR-1 reactor (Novak, 2020). The purpose of the study was to compare a SCRAM transient between experimental and simulated calculations. The experimental data was calculated using point reactor kinetic equations, Eq 6-7. Then reactivity was calculated by solving for $\rho(t)$ as a function of $n(t)$ (Eq 8).

$$\frac{dn}{dt} = \frac{\rho - \beta}{\Lambda} n + \sum_i \lambda_i C_i$$

Eq 6

$$\frac{dC_i}{dt} = \frac{\beta_i}{\Lambda} n - \lambda_i C_i$$

Eq 7

$$\rho(t) = \frac{\Lambda}{n(t)} \cdot \frac{dn(t)}{dt} + \beta - \frac{n_0}{n(t)} \cdot \sum_i \beta_i \cdot e^{-\lambda_i t} - \frac{1}{n(t)} \cdot \sum_i \beta_i \lambda_i \int_t^0 n(tr) \cdot e^{\lambda_i t} dtr$$

Eq 8

The point kinetic equations (PKE) were solved by using a BOKIN code developed by the Department of Nuclear Reactors, FNSPE, and CTU. In comparing the experimental data and the simulated data, there was some discrepancy when using local detectors. This suggested that control rod worth is higher in detectors which are positioned lower in a reactor (Novak, 2020). Moreover, there is another problem with solving the control rod worth using Reactimeter. The three different discrimination settings do not include delayed neutrons. It was concluded that the Serpent dynamic tool is accurate for determining kinetic behavior.

3.7 Homogenization of reactors

Fejt and Frybort (2018) developed a method of cross-section homogenization for small-scale reactors using a combination of Serpent and PARCS. Serpent uses an out-scatter approximation for transport, which assumes in-scatter (Eq 9) to be equivalent. However, this is

not an appropriate approximation for small-scale reactors. Since v2.1.27, Serpent considers a correction factor (Eq 10) which subtracts the hydrogen out-scatter cross-section and replaces it with the total transport multiplied by the correction (Eq 11).

$$\Sigma_{tr,g} = \Sigma_{t,g} - \frac{\Sigma_g \Sigma_{s1,g' \rightarrow g} \Phi_{1,g'}}{\Phi_{1,g}}$$

Eq 9

$$f(E) = \frac{\Sigma_{tr}(E)}{\Sigma_t(E)}$$

Eq 10

$$\Sigma_{tr}^{trc} = \Sigma_{tr} - \Sigma_{tr,H} + \Sigma_{t,H} \cdot f(E)$$

Eq 11

$\Sigma_{tr,g}$ is a transport cross-section of energy group g

$\Sigma_{t,g}$ is the total cross-section

$\Sigma_{s1,g' \rightarrow g}$ is the scattering cross section from g' to g

$\Phi_{1,g}$ is the angular flux of energy g

The authors used Serpent to create homogenized cross sections for 2 different fuel assemblies, the reflector, and channels. The data from Serpent was then fed into PARCS to perform a diffusion approximation of the core. The results were compared to a full 3D Serpent calculation.

4.0 Materials and Methods

4.1 Oregon State TRIGA® Reactor

The OSTR is an open pool, 1.1 MW_{thermal} light water reactor with the ability to pulse to more than 2700 MW_{thermal}. It was designed with several inherently safe features. The reactor has several different radiation facilities used for various purposes for irradiation of samples as seen in Figures 1 and 2.

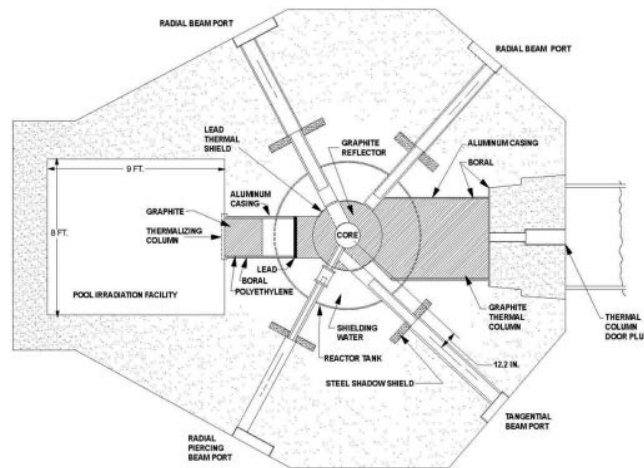


Figure 1: OSTR Horizontal Cross Section (Oregon State University, 2018)

The reactor core is located inside 8 inches of an aluminum-clad graphite reflector, surrounded by 2 inches of lead, 1.5 feet of water moderator radially (16 feet high), and an 8 foot thick concrete biological barrier. This is shown in Figures 1 and 2.

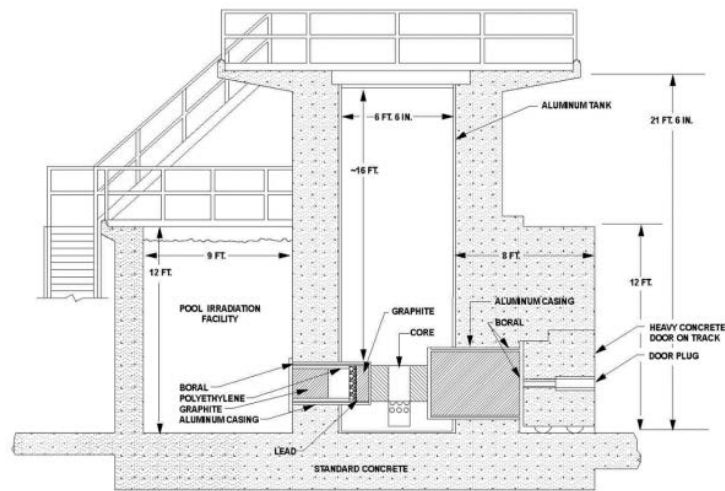


Figure 2: OSTR Vertical Cross Section (Oregon State University, 2018)

The core is composed of fuel, control rods, irradiation facilities, graphite, and a neutron source. Figure 3 shows the arrangement of these rods in the core, and as they are held in place by two grid plates.

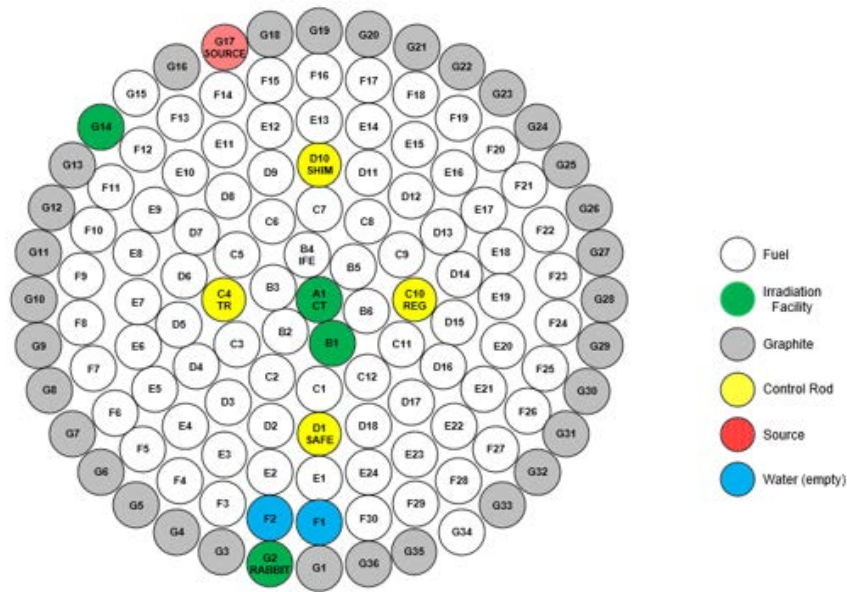


Figure 3: CLICIT core configuration (Oregon State University, 2018)

The upper and lower grid plates in the core consist of an array of aluminum 1.5 diameter inch holes. In total there are 127 lattice locations. Each position is labeled with a letter-number designation for easy identification. The letters designate rings of elements about the center. These are labeled A to G where A is the innermost ring and G is the outermost ring. The number designation refers to the location on the ring. Each ring is numbered, starting from the easternmost direction and moving clockwise. There is a central thimble in lattice position A-1. The control rods, shim, safety, regulating, and transient, are located in positions D-10, D-1, C-10, and C-4 respectively. In position B-1 there is a Cadmium-Lined Inner-Core Irradiation Tube (CLICIT) and in F-20 is a similar Cadmium-Lined Outer-Core Irradiation Tube (CLOCIT). An unlined, In-Core Irradiation Tube (ICIT) is located in position F-12. Finally, the Pneumatic Transfer Tube (Rabbit) is in position G2. All fuel locations are occupied by LEU fuel rods.

Each fuel rod is composed of a mixture of zirconium-hydride, 30 weight % uranium of which 20 % is ^{235}U , and about 1.1 weight % erbium. The rod ends are capped by 3.5 inch graphite slugs and the entire assembly is contained by stainless steel cladding. The design is shown in Figure 4. The erbium acts as a burnable poison, used to smooth the reactivity of the reactor over a period of time as it unproductively absorbs neutrons during the initial loading of the fuel.

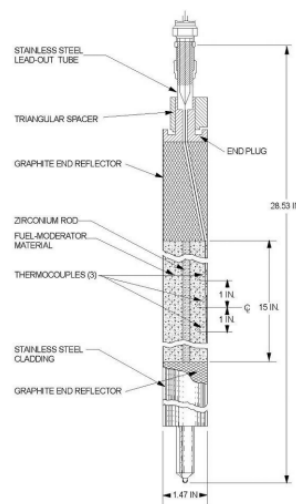


Figure 4: Instrumented Fuel Element (Oregon State University, 2018)

Zirconium-hydride and erbium provide a negative temperature coefficient to the system, reducing the reactivity of the system as the reactor heats up. As the temperature of zirconium-hydride increases, the more likely a scattering event with a low-energy neutron will result in a higher-energy neutron. The higher energy neutrons then have a smaller probability of causing fission in the fuel.

There are four control rods controlling the reactivity of the system: shim, safe, regulating, and transient. Each have a maximum withdrawal height of 15 inches. The first three are composed of, from top to bottom, a graphite slug, 15 inches of a graphite and powdered boron carbide mixture, 15 inches of fuel follower, and a graphite slug. The control rod and fuel follower are shown in Figure 5, with their respective heights relative to the individual fuel rods. The safety, shim, and regulating rods are motor driven, unlike the transient rod which has a pneumatic-electromechanical drive. As such, the transient rod has an air-filled follower.

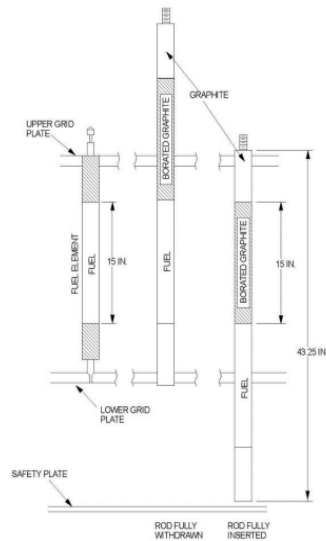


Figure 5: Fuel Element and Control Rod Layout (Oregon State University, 2018)

The transient rod allows for both pulsing and steady-state operation of the reactor. The rod is moved slowly in and out to maintain steady-state conditions. However, during a pulse, the control rod is rapidly withdrawn to the desired height.

The OSTR has several research facilities attached. There are four beam ports (B.P. 1-4) which penetrate the concrete barrier. Both B.P. 1 and 2 face the center of the core and end at the outer edge of the reflector. B.P. 4 also faces the center, but goes further into the core, stopping just inside the assembly. The last beam port is tangential to the core. In addition, there is also a rotating rack surrounding the core.

4.2 Nuclear Reaction Data Library

Nuclear libraries largely refer to available cross-sections for an isotope. As a function of energy, a cross-section shows the probability of interaction, ie: scattering, absorption, and fission. In Serpent, the two primary databases are the Evaluated Nuclear Data File (ENDF) and Joint Evaluated Fission and Fusion File (JEFF). ENDF6 and below have discrete energy cross sections. Newer versions have continuous spectrums.

To address changes to the cross section as a result of atom-to-atom bonding, these libraries also include Thermal Scattering Data. This is significantly important to neutron moderators such as water.

4.3 Critical Rod Configurations

In 2008, after the conversion to LEU fuel, the OSTR ran a control rod calibration. This involved using the Rod Pull Method. This method is used to determine the reactivity change by withdrawing a control rod. In this method, the calibrated control rod being is fully inserted. The

remaining control rods are set to a critical configuration at a power of 15W. The neutron source is removed. The rod is then partially raised to a supercritical state to induce a period between 6 to 15 seconds. From the change in neutron population, the period is calculated by Equation 12. This equation assumes that power and neutron growth are proportional. The remaining control rods are inserted to return the reactor to critical. The procedure is repeated until the rod is fully raised.

$$\frac{P}{P_0} = e^{\frac{t}{T}}$$

Eq. 12

In this equation, P is power, P^0 is the initial power, t is time, and T is the period.

Table 1 is the control rod heights when the reactor was critical during the control rod calibration. This was provided by Robert Schickler, assistant director of the OSTR. Data from Table 1 was used to determine the bias, point-kinetic parameters, and power-per-element for both models.

Table 1: Critical control rod configurations

Trial	Control Rod Heights (%)			
	Transient	Safety	Shim	Regulating
1	24.4	58.7	58.6	59.1
2	36.9	55.7	55.7	54
3	49.2	52	52	49.4
4	61.6	48	48	46.6
5	72.2	44.5	44.5	46.5
6	61	0	61	61.7
7	57.3	26.4	57.4	57.3
8	53.7	40	53.7	53.8
9	50.2	51.7	50.2	50.6
10	46.9	65.8	46.9	46.8
11	63.6	63.6	0	64
12	59.7	59.7	24.7	59.7
13	55.5	55.5	37	55.4
14	51.5	51.5	47.7	52
15	48.1	48	58.7	48.1
16	44.9	44.9	69.6	45
17	68.3	67.8	67.8	0
18	62.9	62.8	62.9	22.1
19	58.3	58.2	58.3	33.5
20	53.9	53.8	53.8	43.3
21	49.7	49.7	49.6	52.9
22	45.8	45.8	45.8	63.4
23	42.3	42.4	42.4	75.3

4.4 Critical Bias

MCNP version 6.2 was used and a previously created model of the OSTR was provided. The endfb7 library was used for the thermal cross-sections. This included lwtr.20t, graph.20t, h-zr.20t, and zr-h.30t for thermal scattering.

Each critical control rod configuration determined above was run to determine their respective deviation from criticality. The mean k_{eff} was then calculated and converted to worth, in dollars (Eq. 13).

$$\$ = \frac{k-1}{k\beta}$$

Eq. 13

In this equation, β is the delayed neutron fraction, which varies for each reactor. In the OSTR, β is approximately 0.0075.

Serpent v2.1.31 was used, but changes to the thermal scattering were applied. This was due to the limitations of this version. The version did not allow for continuous spectrum thermal cross sections such as lwtr.20t. Instead, gre7.00t, lwe7.00t, h/zr.10t, and zr/h.10t were used since they are not continuous. This could lead to some error, because the cross sections of discrete energy ranges are averaged. The next update of Serpent 2 allows for continuous spectrum, but it was unavailable due to export controls.

4.5 Point-Kinetic Parameters

Every fission event releases a variable number of neutrons depending on energy and material. The vast majority of neutrons are prompt and are released within 10^{-14} seconds. Usually, these neutrons have a lifetime of approximately 10^{-4} seconds. Less than 1% of neutrons are delayed, as they are produced by the decay of fission products, but they still significantly contribute to the rate of neutron production. This is because the period in Eq 12 is driven by the average neutron lifetime ($\langle l \rangle$) from Eq 14.

$$T = \frac{\langle l \rangle}{k-1}$$

Eq 14

The average neutron lifetime is estimated by Eq 15.

$$\langle l \rangle = (1 - \beta)l_p + \sum_{i=1}^6 \beta_i \left[\frac{1}{\lambda_i} + l_p \right]$$

Eq 15

In this equation

β_i is the fraction of radioactive fission products that yield a delayed neutron.

β is the sum of β_i such that $(1 - \beta)$ is the fraction of prompt neutrons.

l_p is the prompt neutron lifetime

λ_i is the decay constant of fission products

For ^{235}U the delayed neutron fractions and decay constant are listed in Table 2.

Table 2: Delayed neutron fraction and decay constants

Group (i)	β_i	λ_i (sec ⁻¹)
1	0.038	0.012716
2	0.213	0.031738
3	0.188	0.115525
4	0.407	0.310828
5	0.128	1.397474
6	0.026	3.872331

If a reactor is driven by prompt neutrons, a small deviation from critical would greatly affect the growth of the neutron population. For instance, if k_{eff} were 1.001, the neutron population would double every 0.07 seconds. The presence of delayed neutrons increases the average lifetime to approximately 0.1 sec.

4.6 Experimental Point-Kinetic Parameters

4.6.1 Neutron Lifetime

The OSTR calculated the prompt neutron lifetime (l_p) using the $\frac{1}{v}$ absorber method with MCNP5 (Hartman, 2013). This was done by injecting a small amount of boron into the system model. Using the k eigenvalues from the original system and the borated system, Eq 16 can be solved for the perturbed system,

$$l_p = \frac{1}{N_{B-10} \sigma_a^{B-10} v_0} \left(\frac{k_{ref} - k_p}{k_p} \right)$$

Eq 16

where,

k_{ref} is the k_{eff} of the unperturbed system

k_p is the k_{eff} of the reactor with added boron

$N_{\text{B-10}}$ is the boron 10 density $\left[\frac{\text{atom}}{\text{b cm}} \right]$

v_0 is $220000 \left[\frac{\text{cm}}{\text{s}} \right]$ the speed of a thermal neutron

σ_a^{B-10} is the absorption cross section of boron 10 for a neutron at velocity v_0 ,

3837 [b]

The concentrations used were 7.5×10^{-8} and $1.5 \times 10^{-7} \left[\frac{\text{atom}}{\text{b cm}} \right]$ and the prompt lifetime of the original system was determined by the limit as $N_{\text{B-10}}$ approached zero (Hartman, 2013).

4.6.2 Effective Delayed Neutron Fraction

The delayed neutron fraction was calculated using MCNP5 (Hartman, 2013). The ratio of k_p and k_{p+d} was calculated to determine the prompt neutron fraction. The eigenvalue k_p is determined by assuming all neutrons are born with the prompt energy spectrum; whereas k_{p+d} is the expected distributions of prompt and delayed neutrons.

4.7 MCNP Point-Kinetic Calculations

4.7.1 Neutron lifetime

While MCNP can use the same $\frac{1}{v}$ absorber method, as Hartmen et al. (2013) did, this can be computationally expensive and the uncertainty may be larger than the difference in k (Kiedrowski, 2011). Instead, MCNP uses the average of three estimators: collision, absorption, and track length (X-5, 2008).

"The collision estimator is the average time required for a fission source neutron to be removed from the system." (X-5, 2008) It is shown by Eq. 17 and is based on the expected probabilities of fission.

$$\tau^{col} = \frac{\Sigma W_e T_e + \Sigma (W_c + W_f) T_x}{\Sigma W_e + \Sigma (W_c + W_f)}$$

Eq 17

where

τ^{col} is the collision estimate of the prompt removal lifetime

W_e is the weight of a neutron by escape

T_e is the time until a neutron escapes

W_c is the weight of a neutron lost to a neutron capture at each collision

W_f is the weight of a neutron lost to fission at each collision

and T_x is the time until collision

In this $W_c + W_f$ is determined by Eq. 18

$$W_c + W_f = W_i \sum_j \frac{f_j (\sigma_{cj} + \sigma_{fj})}{\sum_j f_j \sigma_{tj}}$$

Eq 18

where

W_i is the number of neutrons entering collision number i

f_j is the atomic fraction for nuclide j

σ_{cj} is the microscopic capture cross-section of nuclide j

σ_{fj} is the microscopic fission cross section of nuclide j

σ_{tj} is the total microscopic cross-section of nuclide j

The Absorption Estimator (τ^{abs}) is similar to the collision estimator but differs in that it is event-based (X-5, 2008). The lifetime is estimated by Eq. 19.

$$\tau^{abs} = \frac{\sum W_e T_e + \sum (W_c + W_f) T_x}{\sum W_e + \sum W_c + \sum W_f}$$

Eq 19

The track-length estimator (τ^{tl}) is a weighted average time of flight as shown in Eq. 20.

$$\tau^{tl} = \frac{\sum_i W_i \frac{d}{v}}{W_s}$$

Eq 20

where,

d is the distance until an event

v is the speed of the neutron

W_s is the weight of the source.

4.7.2 Effective Delayed Neutron Fraction

The effective delayed neutron fraction is determined by Eq. 22 (X-5, 2008).

$$\beta_{eff} = \frac{N_d}{N_t}$$

Eq 22

This can be viewed as the number of delayed neutrons (N_d) over the total number of neutrons (N_t). A neutron is determined to be delayed by a random roll and Eq. 23.

$$\xi \leq \frac{\frac{v}{v_d}(E)}{\frac{v}{v_t}(E)}$$

Eq 23

If the random roll (ξ) is less than or equal to the ratio of expected delayed neutrons ($\frac{v}{v_d}$) to total expected neutrons ($\frac{v}{v_t}$) at some energy (E), then the neutron is considered delayed.

4.8 Serpent 2 Point-Kinetic Calculations

Serpent 2 estimates the prompt neutron lifetime and delayed neutron fraction using three different approximation methods referred to as Nauchi's, Iterated Fission Probability (IFP), and Perturbation.

4.8.1 Nauchi Neutron Lifetime

Nauchi's method uses collision, absorption, and track length estimators. It was derived from assuming the adjoint flux could be replaced with a next fission probability (Nauchi & Kameyama, 2005b). The implementation is described by Eqs 24-26

$$\tau^{col} = \frac{\sum_{l=1}^S \left(\sum_{j=1}^{j_l} \left(w_j \frac{\sum_k (N_k v_{tk} \sigma_{fk})}{\sum_k (N_k \sigma_{tk})} \sum_{i=1}^j (\Delta t_i) \right) \right)}{S}$$

Eq 24

$$\tau^{abs} = \frac{\sum_{l=1}^S \left(w_j \frac{v_{tk} \sigma_{fk}}{\sigma_{ak}} \sum_{i=1}^j (\Delta t_i) \right)}{S}$$

Eq 25

$$\tau^{trk} = \frac{\sum_{l=1}^S \left(\sum_{j=1}^{j_l} \left(w_j \Delta d_j \sum_k (N_k v_{tk} \sigma_{fk}) \left(\frac{1}{2} \Delta t_j + \sum_{i=1}^{j-1} (\Delta t_i) \right) \right) \right)}{S}$$

Eq 26

where,

j is a collision identifier

k is a nuclide

N_k is the number density

σ_{fk} is the microscopic fission cross section of k

σ_{ak} is the microscopic absorption cross-section of k

σ_{tk} is the total microscopic cross-section of k

v is the velocity of the neutron

Δd is the track length

Δt is the time before an event

and S is the source neutrons

4.8.2 Nauchi Delayed Neutron Fraction

Nauchi & Kameyama (2008) define the delayed neutron fraction as, “the ratio of the number of fission neutrons in the next generation induced by delayed neutrons to that induced by total ones.” The method determines if a neutron is delayed, from Eq 24, before it begins a random walk. If a delayed neutron causes fission, the number of neutrons born is tallied. This score is divided by the total number of neutrons born.

4.8.3 Iterated Fission Probability Neutron Lifetime

The concept of IFP is related to Nauchi's method in the application of the next fission probability. The difference is that IFP traces several generations of neutrons instead of just one. The estimator (Eq 27) only uses neutrons from fissions (Leppänen, 2014).

$$\tau^{\dagger(\lambda)} = \frac{\sum_{k \in (\alpha + \lambda)} l_k^{(-\lambda)} \cdot w_k}{\sum_{k \in (\alpha + \lambda)} w_k}$$

Eq 27

where

α is the initial generation

λ is the total number of neutron generations after α

k is a neutron identifier

$l_k^{(-\lambda)}$ is the neutron lifetime of the ancestors of neutron k

w_k is the weight of neutron k

4.8.4 Iterated Fission Probability Delayed Neutron Fraction

To determine the delayed neutron fraction, each neutron is randomly sampled as in Eq 13 for each precursor group (j). The delayed neutron fraction can be determined by summing all of the delayed groups from Eq 28.

$$\beta_{eff(j)}^{(\lambda)} = \frac{\sum_{k \in (\alpha + \lambda)} w_k \cdot \delta_{g_k}^{(-\lambda)}}{\sum_{k \in (\alpha + \lambda)} w_k}$$

Eq 28

In this equation, $\delta_{g_k^{(-\lambda)}}$ is one for a neutron in group j and zero otherwise. For instance, if j is zero, representing prompt neutrons, then only sampled prompt neutrons would be one. This is similar to MCNP but is more generalized to include several generations and delayed groups.

4.8.5 Perturbation Neutron Lifetime

Perturbation estimations come from changing the unbiased sampling of events through variance reduction schemes. Serpent 2 uses delta tracking which alters the probability distribution through a rejection scheme. The method uses the IFP and changes the relative weight $\frac{\partial w_n}{w_n}$ of a particle n for event x by Eq 29 (Aufiero et al., 2015).

$$\frac{\frac{\partial w_n}{w_n}}{\frac{\partial x}{x}} = \sum_{g=(\alpha-\lambda)}^{\alpha} ({}^{(n,g)}ACC_x - {}^{(n,g)}REJ_x)$$

Eq 29

ACC is an accepted event in generation g and REJ is a rejected one.

The change in weights alters Eq 27 into Eq 30.

$$\tau^{\dagger(\lambda)} = \frac{\left(\frac{\sum_{k \in (\alpha+\lambda)} w_k \left[\sum_{g=(\alpha-\lambda)}^{\alpha+\lambda} ({}^{(n,g)}ACC_x - {}^{(n,g)}REJ_x) \right] l_k^{(-\lambda)}}{\sum_{k \in (\alpha+\lambda)} w_k \cdot l_k^{(-\lambda)}} \right)}{\left(\frac{\sum_{k \in (\alpha+\lambda)} w_k \left[\sum_{g=(\alpha-\lambda)}^{\alpha+\lambda} ({}^{(n,g)}ACC_x - {}^{(n,g)}REJ_x) \right] l_k^{(-\lambda)}}{\sum_{k \in (\alpha+\lambda)} w_k \cdot l_k^{(-\lambda)}} \right)}$$

Eq 30

The numerator can be seen as the average net events weighted on the lifetimes whereas the denominator is just the average net number of events.

4.8.6 Perturbation Neutron Fraction

Just as with all methods, perturbation rolls to determine if a neutron is delayed

(d). The method then calculates the effective delayed neutron fraction using Eq 31.

$$\beta_{eff}^{(\lambda)} = \frac{\left(\frac{\sum_{k \in (\alpha+\lambda)} w_k \left[\sum_{g=(\alpha-\lambda)}^{\alpha+\lambda} ({}^{(n,g)}ACC_x - ({}^{(n,g)}REJ_x) \right] \cdot \delta_{g_k}^{(-\lambda)}}{\sum_{k \in (\alpha+\lambda)} w_k \cdot \delta_{g_k}^{(-\lambda)}} \right)}{\left(\frac{\sum_{k \in (\alpha+\lambda)} w_k \left[\sum_{g=(\alpha-\lambda)}^{\alpha+\lambda} ({}^{(n,g)}ACC_x - ({}^{(n,g)}REJ_x) \right]}{\sum_{k \in (\alpha+\lambda)} w_k} \right)}$$

Eq 31

4.9 Experimental Rod Worth Calibration

The control rod worths were determined by the Rod Pull Method described earlier. After each pull, a period is induced. Using the Inhour equation (Eq 32), reactivity can be calculated from the period. From reactivity, the rod worth is simply calculated by dividing by the delayed neutron fraction (Eq. 33). Since this method calculates the rod worth in sections, the integral rod worth is determined by the sum from fully inserted to the current rod height.

$$\rho = \frac{l_0}{T} + \sum_{i=1}^6 \frac{\beta_i}{1+\lambda_i T}$$

Eq 32

The inhour equation to solves for reactivity (ρ) using the prompt neutron lifetime (l^0), the period, the decay constant of fission fragments (λ_i), the fraction of neutron from the fission fragments (β_i), and the reactor period (T).

$$\beta = \frac{\rho}{\beta_d}$$

Eq 33

4.10 MCNP/Serpent Rod Worth Calculation

The supercritical rod heights and reactor periods from the calibration were taken from log books. These heights were then used in the models to generate k_{eff} directly. Table 3 shows the control rod heights used for each rod calibration. The supercritical heights from the data change only the height of the rod being calibrated. This allows for direct calculation of the rod's worth as opposed to needing a stepwise integral calculation.

Table 3: Control rod calibration configurations

Calibration Rod	Control Rod Height (%)			
	trans	safe	shim	reg
transient	24.4	63.1	63.1	63.1
	36.9	63.1	63.1	63.1
	49.2	63.1	63.1	63.1
	61.6	63.1	63.1	63.1
	72.2	63.1	63.1	63.1
	100	63.1	63.1	63.1
safe	61	26.4	61	61.7
	61	40	61	61.7
	61	51.7	61	61.7
	61	65.8	61	61.7
	61	100	61	61.7
shim	63.6	63.6	24.7	64
	63.6	63.6	37	64
	63.6	63.6	47.7	64
	63.6	63.6	58.7	64
	63.6	63.6	69.6	64
	63.6	63.6	100	64
reg	68.3	67.8	67.8	22.1
	68.3	67.8	67.8	33.5
	68.3	67.8	67.8	43.3
	68.3	67.8	67.8	52.9
	68.3	67.8	67.8	63.4
	68.3	67.8	67.8	75.3
	68.3	67.8	67.8	100

4.11 Shutdown Margin and Core Excess

The shutdown margin is the reactivity difference between a critical reactor and a complete shutdown system. This is determined by running the reactor model with all control rods fully inserted.

Similarly, core excess is the difference between a critical reactor and a system with all of the control rods withdrawn.

The relationship between rod worth, core excess, and the shutdown margin is demonstrated in Figure 6. To further check the capability of both models for solving the neutron transport system, the total rod worth is compared to the core excess minus the shutdown margin.

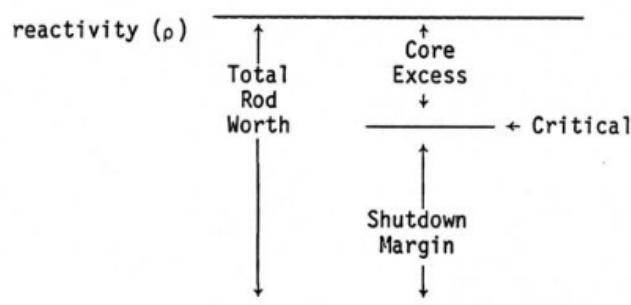


Figure 6: Total rod worth compared to core excess and shutdown margin (Oregon State University, 2018)

4.12 Power Per Element

MCNP calculates the energy of a cell by estimating the flux through a direct tally. The user sets pseudo neutron detectors (f card) at each fuel rod cell using either f-tally cards, 4 (flux) or 6 (energy). A tally multiplier, fm card is used for an F4 detector to convert the flux directly into energy. Both methods solve Equation 15. The F4 method was used paired with fm4

-1.2352e04 5401 (-6 -8). The values following fm4 indicate density, the material identifier, and the response function for calculating energy in W/cc.

Serpent uses a combination of surface tracking and collision estimations to determine the flux of the system. The collision estimator, R_{cfe} , is a summation of all collisions inside a region over the material cross-section, Σ_{tot} as seen in Eq 34. The collision estimator runs into issues in regions of low density or voids. One solution is to allow for the code to score virtual collisions, however this may significantly increase computation time. The code only allows for this when the material cross-section falls below a predefined threshold. The collision estimator is used in most cases, but can be switched to surface tracking if the Eq 5 is lower than another threshold (Leppänen, 2010).

$$R_{cfe} = \sum_{i=1}^l \frac{f_i}{\Sigma_{tot,i}}$$

Eq 34

In surface tracking, the neutron path length of the material cross-section is sampled and neutrons crossing the boundary are stopped at the surface.

4.13 Temperature Coefficient of Reactivity

The temperature of the materials in the core can greatly affect the reactivity of the system because their cross-sections and densities are dependent on energy. For instance, zirconium-hydride has a negative temperature coefficient as stated in the fuel description section.

Both MCNP and Serpent 2 ran trial 1 from Table 1 at 293, 400, 500, and 600 K. The slope of the linear fitted line represents the change in reactivity as a function of temperature.

5.0 Results

5.1 MCNP and SERPENT 2 Bias

The MCNP and Serpent 2 OSTR models both accurately predict critical reactor conditions as seen in Table 4.

Table 4: Critical Bias Trial Results

Trial	k_{eff}	
	MCNP	SERPENT 2
1	0.99999 ± 0.00032	1.0003 ± 0.00035
2	0.99977 ± 0.00035	0.9998 ± 0.00027
3	1.00098 ± 0.00033	1.0003 ± 0.0003
4	1.00022 ± 0.00038	1.0007 ± 0.00029
5	1.00111 ± 0.0003	1.0001 ± 0.00031
6	1.00131 ± 0.0003	1.0014 ± 0.00035
7	1.00006 ± 0.00033	1.0004 ± 0.00032
8	1.00025 ± 0.00034	1.0009 ± 0.00032
9	1.00035 ± 0.00032	1.0001 ± 0.00029
10	1.0003 ± 0.00034	1.0005 ± 0.00036
11	1.00098 ± 0.0003	1.0003 ± 0.00031
12	1.00041 ± 0.0003	1.0003 ± 0.00032
13	0.99846 ± 0.00029	1.0003 ± 0.00037
14	1.00042 ± 0.00029	1.0006 ± 0.00031
15	1.00017 ± 0.00038	1.0000 ± 0.0003
16	1.00023 ± 0.00035	1.0004 ± 0.00031
17	1.0015 ± 0.00031	1.0020 ± 0.00037
18	1.00184 ± 0.0003	0.9999 ± 0.00033
19	1.00116 ± 0.00031	1.0005 ± 0.00031
20	1.00055 ± 0.00029	1.0004 ± 0.00033
21	0.99955 ± 0.0003	1.0003 ± 0.00035
22	0.9997 ± 0.00036	1.0002 ± 0.00032
23	0.99966 ± 0.0003	1.0001 ± 0.00033

The MCNP model's bias was calculated to be 0.05 ± 0.11 . Similarly, the Serpent 2 model bias was calculated to be 0.06 ± 0.08 . Both models are found to be well within one standard deviation for a critical reactor. None of the individual trials were outside of one standard deviation. In terms of the k-eigenvalue, Serpent 2 only differs from MCNP by approximately 0.004%.

5.2 Point-Kinetic Parameters

The difference between MCNP and Serpent is within the accepted standard deviation of MCNP when calculating the delayed neutron fraction, as seen in Table 5. Each of the Serpent methods runs low and has a standard deviation an order of magnitude lower than MCNP. IFP appears to be the best approximation for the real-world value of the delayed neutron fraction.

The MCNP calculation of the prompt neutron lifetime is high and outside the range of the previous experiments. The measured values were derived using the $\frac{1}{\beta}$ method through MCNP whereas MCNP approximates using alternate methods as discussed in the materials and methods section. Serpent predicts the lifetime better overall. Perturbation theory appears to accurately predict the lifetime.

Table 5: Point-Kinetic Parameter results

Method	delayed neutron fraction	prompt neutron lifetime (s)
MCNP	0.00741 ± 0.00061	0.0000280 ± 0.0000010
Serpent Nauchi's	0.00716 ± 0.00005	0.0000240 ± 0.0000001
Serpent IFP	0.00732 ± 0.00019	0.0000213 ± 0.0000002
Serpent Pertubation	0.00724 ± 0.00008	0.0000225 ± 0.0000001
Measured	0.00760 ± 0.0001	0.0000226 ± 0.0000029

5.3 Rod Worth

The rod worth from both models was comparable to the measured values in Appendix A. Figures 7-11 show the rod worth as a function of percent withdrawn. There is little difference between MCNP, Serpent 2, and measured values. From the data, most predictions are within one standard deviation. Error bars have been provided as \$0.12 for MCNP and \$0.091 for Serpent 2, which is the largest error for each.

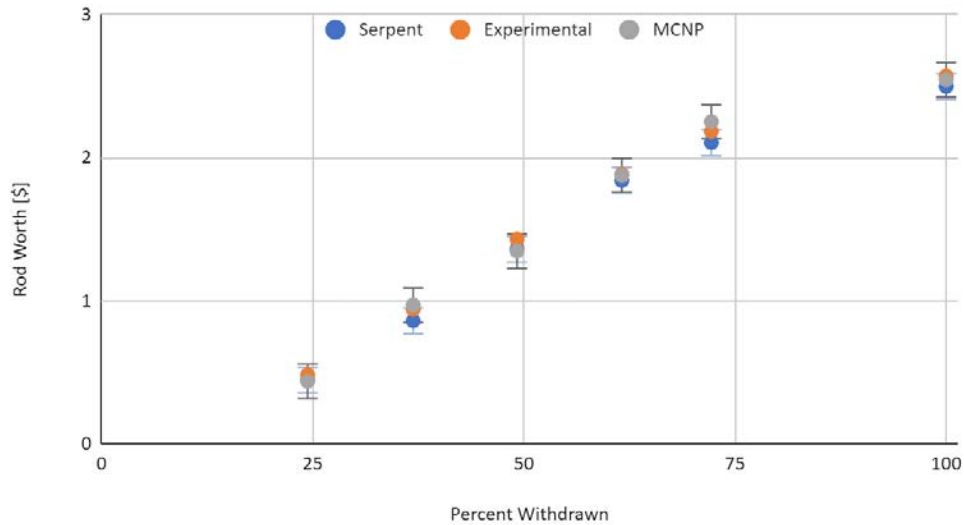


Figure 7: Transient rod worth vs percent withdrawn

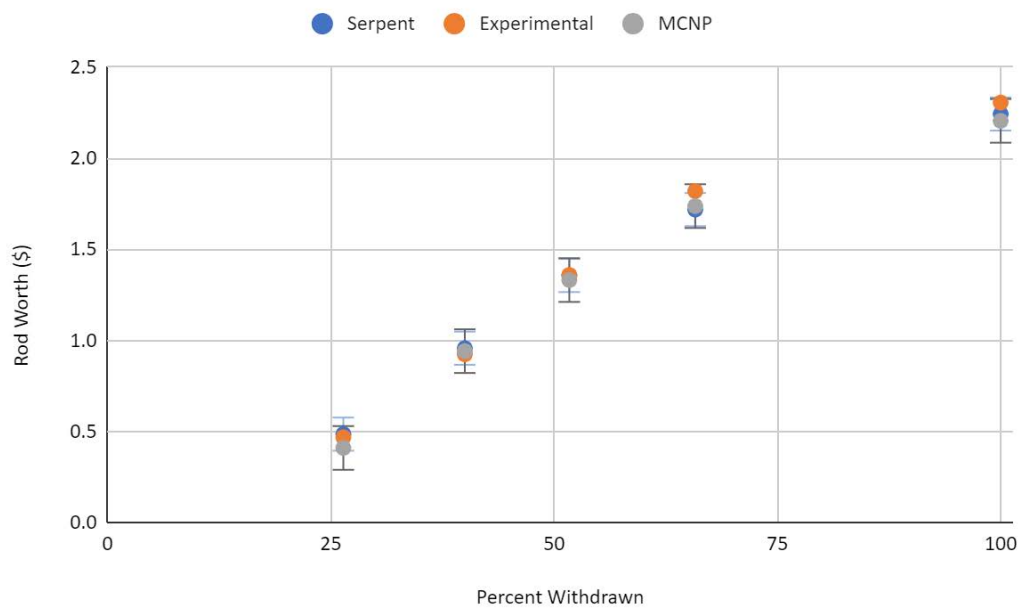


Figure 8: Safe rod vs percent withdrawn

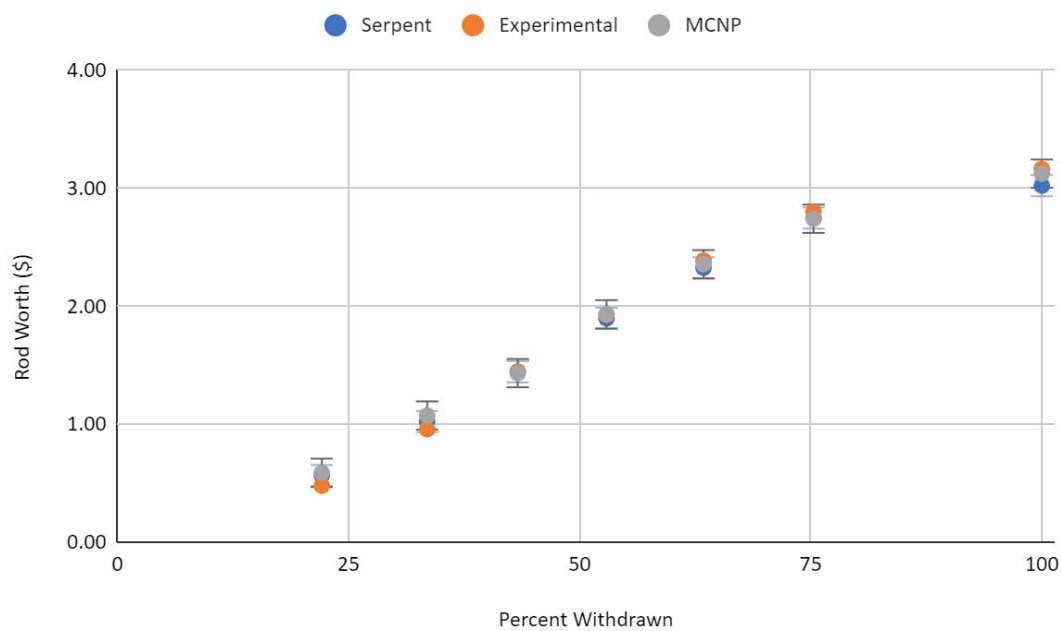


Figure 9: Reg rod vs percent withdrawn

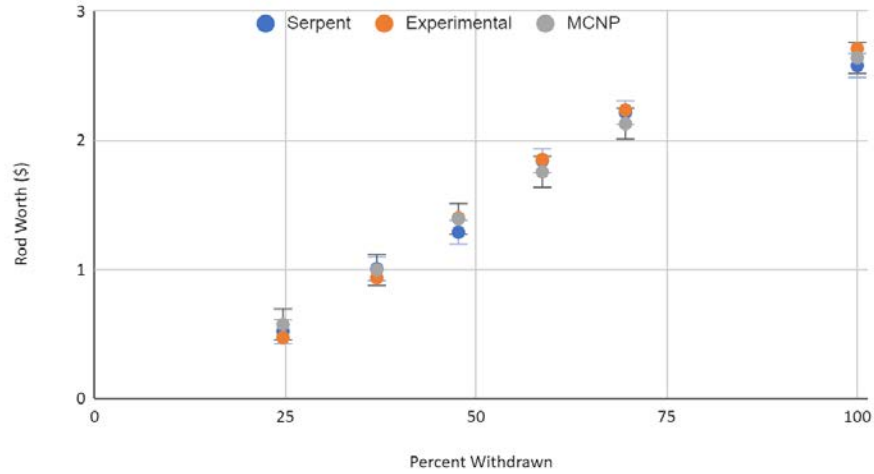


Figure 10: Shim rod vs percent withdrawn

5.4 Core Excess and Shutdown Margin

The core excess and shutdown margin were determined and can be referred to in Table 6. MCNP and Serpent were nearly identical, but still lower than the initial LEU benchmark tests (Hartman 2013). Hartman saw similar results and speculated it to be a result of fuel composition, model bias, or core configuration

Table 6: Core excess and shutdown margin results.

Evaluation	Method	Worth (\$)
core excess	MCNP	4.68 ± 0.12
	Serpent	4.64 ± 0.09
	Measured	7.12 ± 0.35
shutdown margin	MCNP	-6.60 ± 0.12
	Serpent	-6.72 ± 0.09

The core excess was combined with the shutdown margin and compared to the total rod worth. Referring to Figure 6, these two calculations should be equivalent. The results are shown below in Table 7

Table 7: Core excess and shutdown margin as compared to the total rod worth

Evaluation	Method	Worth (\$)
Core Excess/Shutdown Margin	MCNP	11.28 ± 0.16
	Serpent 2	11.36 ± 0.12
Total Rod Worth	MCNP	10.51 ± 0.24
	Serpent 2	10.34 ± 0.18
	Measured	10.75

The difference between the combined core excess and shutdown margin to total rod worth is $\$0.77 \pm 0.3$ and $\$1.02 \pm 0.2$. This would indicate an increased error associated with extreme k-eigenvalue calculations. However, both MCNP and Serpent 2 were within one standard deviation of each other.

5.5 Power Per Element

5.5.1 Side by Side Comparison

The power per element was determined for MCNP and Serpent. Figures 11 and 12 below show the power generated by the TRIGA® reactor at 1 MW determined by MCNP and Serpent 2 respectively. For this critical configuration 3, the element that had the maximum power generated is B4 at 14.92 kW and the minimum element is F13 at 8.28 kW. Appendix B shows the calculated power per element for all fuel elements.

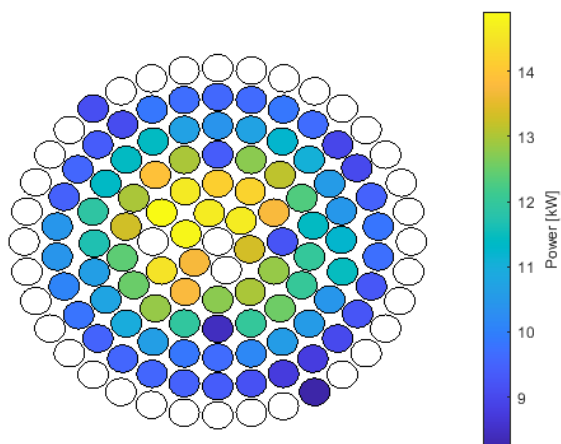


Figure 11: MCNP power per element for trial 3: trans at 49.2,

safe at 52 shim at 52, and reg at 49.4

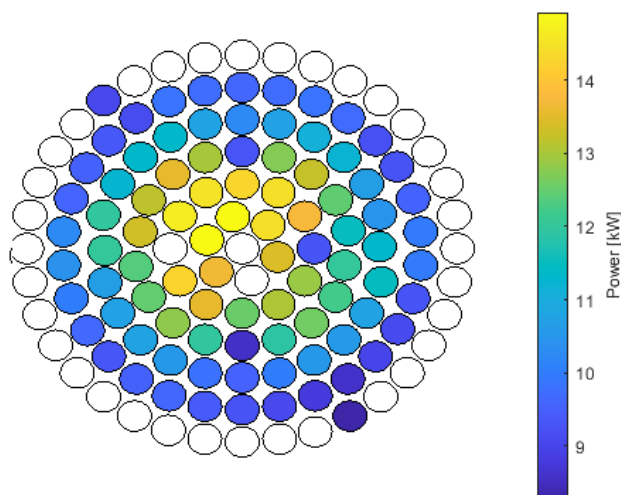


Figure 12: Serpent 2 power per element for trial 3: trans at 49.2,

safe at 52 shim at 52, and reg at 49.4

Other configurations yielded similar results with the maximum element moving about the b-ring and, occasionally, the c-ring.

5.5.2 Mean and Maximum Difference

The difference between Serpent 2 and MCNP was calculated. Figures 13 and 14 illustrate the absolute maximum difference and the average difference for each element between MCNP and Serpent. The exact values for each element can be found in Appendix C.

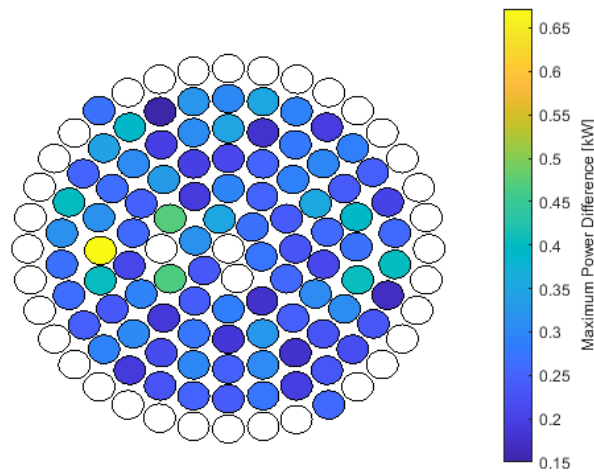


Figure 13: Maximum power difference per element between MCNP and Serpent

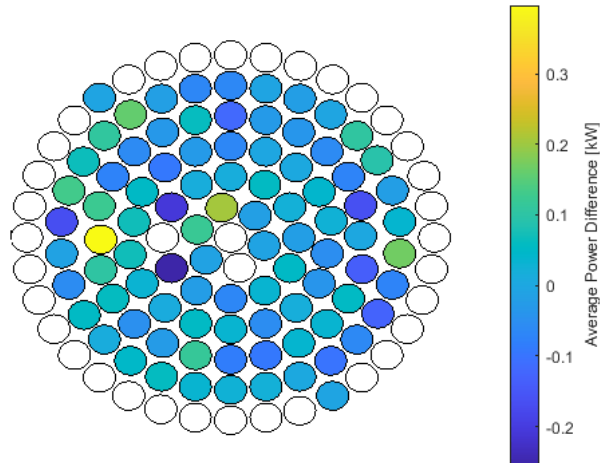


Figure 14: Average power difference per element between MCNP and Serpent

The largest difference between Serpent and MCNP is 0.7 kW at E7. This occurred for trial 4 (reference critical trials). E7 has the largest absolute average difference of 0.4 kW. By inspection of Figure 13 and 14, the fuel rods surrounding the transient rod appear to have the largest error associated with them.

5.6 Temperature Coefficient of Reactivity

The data represented in Figure 15 shows agreement between MCNP and Serpent 2. They show that for every degree K in temperature, the reactor loses about \$0.01 in reactivity. More specifically, MCNP predicts a loss of 0.0108 ± 0.0009 and Serpent 2 predicts 0.0104 ± 0.001 . The data obtained are shown in Table 8.

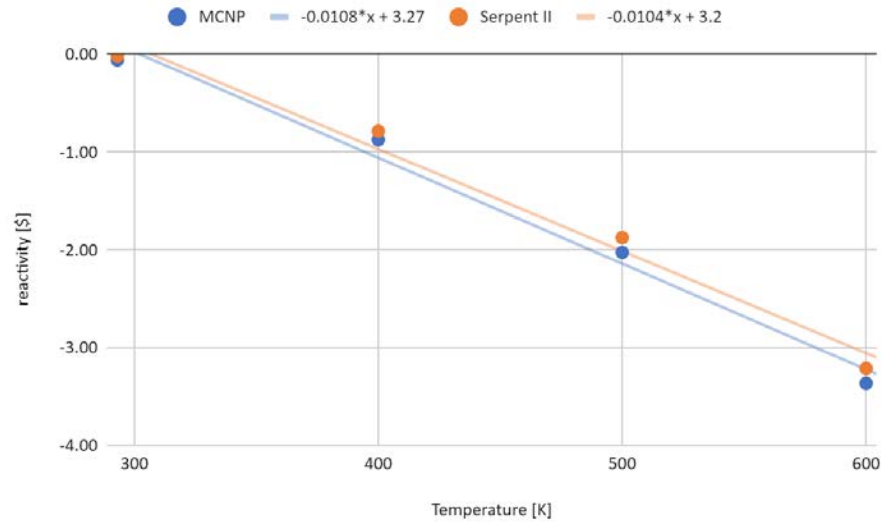


Figure 15: Reactivity vs Temperature.

Table 8: Reactivity at different temperatures

Temp (K)	MCNP	Serpent 2
	Reactivity (\$)	Reactivity (\$)
293	-0.06 ± 0.04	-0.02 ± 0.05
400	-0.87 ± 0.04	-0.78 ± 0.05
500	-2.03 ± 0.05	-1.87 ± 0.04
600	-3.37 ± 0.04	-3.21 ± 0.04

6.0 Discussion

Building a model in Serpent is similar to MCNP. Translating code from MCNP to Serpent was almost trivial as the syntax is nearly identical. Both solve the steady-state transport equation with probabilistic methods. The largest difference between the two is the applied sampling method. MCNP uses a stepwise approach, tracking neutrons from material to material,

and checking for collisions. Serpent uses Delta Tracking to test for a virtual collision using the majorant cross-section; it then tests for a true collision by comparing the true cross-section of the material and the majorant. Delta Tracking has the potential to be a more efficient method with some limitations.

The MCNP OSTR model was developed and refined to accurately calculate the criticality of the reactor and the worth of its assemblies. This made it well suited to translate into Serpent 2 code.

Both models accurately predicted the response of the TRIGA® reactor for most parameters. The critical bias between each model is nearly identical and well within the standard deviation. The point-kinetic parameters appear within reason as well. The MCNP delayed neutron fraction is within one standard deviation of the accepted value. Serpent 2 was not within the standard deviation for any method, but IFP was within two. On the other hand, Serpent 2 approximates the prompt neutron lifetime very well, while MCNP overestimates the lifetime. This is likely due to inherent bias in the approximations, including the accepted results from Hartmen et al. (2013). This is not overly concerning as these fall within previously and currently accepted values. For reference, the HEU core used a β_{eff} of 0.007 some time before Hartmen et al. (2013) calculated it to be 0.0076.

The worth of all control rods was accurately predicted with both models. There does not appear to be any significant difference. Both models were well in agreement with the measured worth for all data points. However, core excess was well below the measured value for both

MCNP and Serpent 2. As stated by Hartman et al. (2013), this is likely due to model bias, core configuration, or fuel material composition. It is unlikely model bias influenced the results as this study calculated the bias to be much less than the error in core excess. Core configuration may still be part of the error. The initial core excess calculated via MCNP was done before the core layout was finalized. The fuel composition is possible because the manufacturer only supplied the mass spectroscopy data of one element, which assumed to be the same for the rest (Hartman et al, 2013).

The power-per-element calculations between the two models are similar. The elements around the transient rod were the largest concern as they have the largest average difference, specifically E7. This may be due to the rejection bias of the delta tracking method due to the air follower of the transient rod. It might also be due to not applying the transformation, raising the control rod, in the model appropriately. However, an error of 0.4 kW is approximately a 3% difference.

Similarly, the largest difference occurs at E7 in trial 12 at 0.7 kW. This was calculated to be about a 5% difference, still considered minimal even though it is outside of two standard deviations of the element's average, 0.40 ± 0.12 kW. This may also be due to human error by not appropriately changing the model for that specific trial, since the average is low and consistent.

7.0 Conclusion

A model of the OSTR was developed in Serpent 2 by translating an accepted MCNP model. Both codes were verified and validated through comparison to each other and data gathered from the LEU core start-up.

Compared to criticality measurements, the reactor bias for both models was determined to be well within acceptable limits. For MCNP and Serpent 2, respectively, the bias was calculated to be 0.05 ± 0.11 and 0.06 ± 0.08 . Both programs accurately predicted neutron lifetime, and rod worth. There was error associated with core excess and shutdown margin; however, the models were in agreement with each other. This could be a result of uncertainties in material composition.

Both MCNP and Serpent 2 also agreed on other parameters that weren't measured. The results from the delayed neutron fraction, power per element, and temperature coefficient were generally within one standard deviation of each other. There was some error seen in calculating the power generated by the fuel follower in the regulating rod for one trial. No other significant differences are apparent between the two model results.

For the OSTR, there is little to no difference between both MCNP and Serpent 2 for steady-state calculations. The MCNP model is already in use and widely accepted as an accurate representation of reactor physics. This work justifies Serpent to be treated as equivalent to MCNP for any future steady-state calculations.

8.0 Future Work

This research project largely follows the methodology performed by Hartman, et al. (2013). There were a few experiments not performed due to time constraints and relative importance. These include the fuel burnup, void coefficient, moderator temperature coefficient of reactivity, and the xenon effect on reactivity.

The biggest purpose of moving from MCNP to Serpent 2 is the transient capabilities. The OSTR can pulse, and being able to model that virtually would be beneficial. The next step would be to compare time-dependent features to real-world experiments. This would further validate the Serpent model.

9.0 References

- A. Sood. The Monte Carlo Method and MCNP - A Brief Review of Our 40 Year History. Los Alamos National Laboratory Presentation LA-UR-17-25633. Los Alamos, NM, USA. 2017.
- Aufiero, M., Bidaud, A., Hursin, M., Leppänen, J., Palmiotti, G., Pelloni, S., & Rubiolo, P. (2015). A collision history-based approach to sensitivity/perturbation calculations in the continuous energy Monte Carlo code SERPENT. *Annals of Nuclear Energy*, 85, 245–258. <https://doi.org/10.1016/j.anucene.2015.05.008>
- Baik, S.-H. (1999). *Feasibility study on the medical isotopes production with solution target using OSTR: ^{99}Mo and related isotopes*.
- Brown, D. A., Chadwick, M. B., Capote, R., Kahler, A. C., Trkov, A., Herman, M. W., Sonzogni, A. A., Danon, Y., Carlson, A. D., Dunn, M., Smith, D. L., Hale, G. M., Arbanas, G., Arcilla, R., Bates, C. R., Beck, B., Becker, B., Brown, F., Casperson, R. J., ... Zhu, Y. (2018). ENDF/B-VIII.0: The 8 th Major Release of the Nuclear Reaction Data Library with CIELO-project Cross Sections, New Standards and Thermal Scattering Data. *Nuclear Data Sheets*, 148, 1–142. <https://doi.org/10.1016/j.nds.2018.02.001>
- Castagna, C., Chiesa, D., Cammi, A., Boarin, S., Previtali, E., Sisti, M., Nastasi, M., Salvini, A., Magrotti, G., & Prata, M. (2018). A new model with Serpent for the first criticality benchmarks of the TRIGA Mark II reactor. *Annals of Nuclear Energy*, 113, 171–176. <https://doi.org/10.1016/j.anucene.2017.11.011>
- Fejt, F., & Frybort, J. (2018). Analysis of a small-scale reactor core with PARCS/Serpent. *Annals of Nuclear Energy*, 117, 25–31. <https://doi.org/10.1016/j.anucene.2018.03.002>

- Galeana, J. H., Aragon, J. G., Torres, A. G., & López, C. F. (2019). Fuel loading, criticality and control rod worth calculations of the Triga Mark III reactor using Serpent and MCNP. *International Journal of Nuclear Energy Science and Technology*, 13(1), 38.
<https://doi.org/10.1504/ijnest.2019.099707>
- Hartman, M. R., Keller, S. T., Reese, S. R., Robinson, B., Stevens, J., Matos, J. E., Marcum, W. R., Palmer, T. S., & Woods, B. G. (2013). Neutronic analysis of the Oregon State TRIGA reactor in support of conversion from HEU fuel to LEU fuel. *Nuclear Science and Engineering*, 174(2), 135–149. <https://doi.org/10.13182/nse12-5>
- Hummel, A. J. (2013). *Molybdenum-99 production in the Oregon State TRIGA reactor : Analysis of the reactor design using a new LEU target as fuel*. Oregon State University, 2014.
- Kiedrowski, B. C., Brown, F. B., & Wilson, P. P. H. (2011a). Adjoint-Weighted Tallies fork-Eigenvalue Calculations with Continuous-Energy Monte Carlo. *Nuclear Science and Engineering*, 168(3), 226–241. <https://doi.org/10.13182/nse10-22>
- Kiedrowski, B. C., Brown, F. B., & Wilson, P. P. H. (2011b). Adjoint-Weighted Tallies fork-Eigenvalue Calculations with Continuous-Energy Monte Carlo. *Nuclear Science and Engineering*, 168(3), 226–241. <https://doi.org/10.13182/nse10-22>
- Kitto, A. K. (2012). *Determination of a calculation bias in the MCNP model of the OSTR*. Oregon State University, 2013.
- Leppänen, J. (2013). *Development of a Dynamic Simulation Mode in Serpent 2 Monte Carlo Code.*, *M&C*, 117–127.
- Leppänen, J. (2015). *a Continuous-energy Monte Carlo Reactor Physics Burnup Calculation Code*. *VTT Technical Research Centre of Finland*.

- Leppänen, J. (2017). On the use of delta-tracking and the collision flux estimator in the Serpent 2 Monte Carlo particle transport code. *Annals of Nuclear Energy*, 105, 161–167.
<https://doi.org/10.1016/j.anucene.2017.03.006>
- Leppänen, J. (2019). Response matrix method–based importance solver and variance reduction scheme in the serpent 2 monte carlo code. *Nuclear Technology*, 205(11), 1416–1432.
<https://doi.org/10.1080/00295450.2019.1603710>
- Leppänen, J., Aufiero, M., Fridman, E., Rachamin, R., & van der Marck, S. (2014). Calculation of effective point kinetics parameters in the Serpent 2 Monte Carlo code. *Annals of Nuclear Energy*, 65, 272–279. <https://doi.org/10.1016/j.anucene.2013.10.032>
- Leppänen, J., Pusa, M., Viitanen, T., Valtavirta, V., & Kaltiaisenaho, T. (2015). The serpent monte carlo code: Status, development and applications in 2013. *Annals of Nuclear Energy*, 82, 142–150.
- Lyons, J. (2013). *Reactor physics model of the Advanced Test Reactor using TRIGA® fuel through application of Serpent 2*.
- Nauchi, Y., & Kameyama, T. (2005a). Proposal of Direct Calculation of Kinetic Parameters β_{eff} and Based on Continuous Energy Monte Carlo Method. *Journal of Nuclear Science and Technology*, 42(6), 503–514. <https://doi.org/10.1080/18811248.2004.9726417>
- Nauchi, Y., & Kameyama, T. (2005b). Proposal of Direct Calculation of Kinetic Parameters β_{eff} and Based on Continuous Energy Monte Carlo Method. *Journal of Nuclear Science and Technology*, 42(6), 503–514. <https://doi.org/10.1080/18811248.2004.9726417>
- Novak, O., Sklenka, L., Fejt, F., Maldonado, I., & Chvala, O. (2020). Rod drop transient at VR-1 reactor – Experiment and Serpent transient calculation analysis. *Annals of Nuclear Energy*, 141, 107296. <https://doi.org/10.1016/j.anucene.2019.107296>

Oregon State University. (2018). *Oregon State TRIGA Reactor Training Manual*.

Schickler, R. A., Marcum, W. R., & Reese, S. R. (2013). Comparison of HEU and LEU neutron spectra in irradiation facilities at the Oregon State TRIGA® Reactor. *Nuclear Engineering and Design*, 262, 340–349. <https://doi.org/10.1016/j.nucengdes.2013.05.004>

Woodcock, E. R., Murphy, T., Hemmings, P. J., & Longworth, T. C. (1965). Techniques used in the GEM code for Monte Carlo neutronics calculations in reactors and other systems of complex geometry. *ANL-7050*. Argonne National Laboratory.

X-5 Monte Carlo Team. (2008). *MCNP — A General Monte Carlo N-Particle Transport Code* (Vol. 1). Los Alamos National Laboratory. (Original work published 2003)

10.0 Appendix

Appendix A

Rod worth calibration data

Calibration rod	Control Rod Height (%)	Rod Worth (\$)		
		MCNP	Serpent 2	measured
transient	24.4	0.44 ± 0.11	0.44 ± 0.09	0.48
	36.9	0.97 ± 0.12	0.86 ± 0.09	0.94
	49.2	1.35 ± 0.12	1.36 ± 0.09	1.43
	61.6	1.88 ± 0.12	1.84 ± 0.09	1.88
	72.2	2.25 ± 0.12	2.10 ± 0.09	2.18
	100	2.54 ± 0.12	2.50 ± 0.09	2.57
safe	26.4	0.41 ± 0.12	0.48 ± 0.09	0.47
	40	0.94 ± 0.12	0.96 ± 0.09	0.92
	51.7	1.33 ± 0.12	1.36 ± 0.09	1.36
	65.8	1.74 ± 0.12	1.72 ± 0.09	1.82
	100	2.21 ± 0.12	2.24 ± 0.09	2.31
shim	24.7	0.57 ± 0.12	0.52 ± 0.09	0.47
	37	1.00 ± 0.12	1.01 ± 0.09	0.94
	47.7	1.39 ± 0.12	1.29 ± 0.09	1.40
	58.7	1.76 ± 0.12	1.84 ± 0.09	1.85
	69.6	2.13 ± 0.12	2.22 ± 0.09	2.24
	100	2.64 ± 0.12	2.58 ± 0.09	2.71
reg	22.1	0.59 ± 0.12	0.56 ± 0.09	0.48
	33.5	1.07 ± 0.12	1.02 ± 0.09	0.96
	43.3	1.43 ± 0.12	1.44 ± 0.09	1.45
	52.9	1.93 ± 0.12	1.90 ± 0.09	1.93
	63.4	2.36 ± 0.12	2.33 ± 0.09	2.39
	75.3	2.74 ± 0.12	2.75 ± 0.09	2.80
	100	3.12 ± 0.12	3.02 ± 0.09	3.16

Appendix B

Power per element calculation for Trial 3: trans at 49.2%, safe at 52%, shim at 52%, and reg at 49.4%. The choice to publish this trial is simply due to all the rod heights being similar.

Element	MCNP	Serpent	Difference	Difference (%)
b2	13.720	13.671	-5.0E-02	0.36
b3	14.834	14.922	8.8E-02	0.59
b4	14.652	14.922	2.7E-01	1.84
b5	14.648	14.431	-2.2E-01	1.48
b6	13.329	13.429	1.0E-01	0.75
c1	12.756	12.540	-2.2E-01	1.70
c2	13.769	13.560	-2.1E-01	1.52
c3	14.492	14.249	-2.4E-01	1.68
c5	14.914	14.661	-2.5E-01	1.69
c6	14.616	14.506	-1.1E-01	0.76
c7	14.176	14.287	1.1E-01	0.78
c8	14.229	14.452	2.2E-01	1.57
c9	13.744	13.744	4.9E-04	0.00
c10	9.215	9.284	6.9E-02	0.74
c11	12.826	12.878	5.2E-02	0.41
c12	12.979	13.046	6.6E-02	0.51
d1	8.445	8.572	1.3E-01	1.50
d2	11.952	11.976	2.4E-02	0.20
d3	12.823	12.815	-7.6E-03	0.06
d4	12.519	12.507	-1.2E-02	0.09
d5	12.405	12.370	-3.5E-02	0.28
d6	13.293	13.315	2.3E-02	0.17
d7	12.977	13.173	2.0E-01	1.51
d8	13.896	13.563	-3.3E-01	2.39
d9	13.000	12.996	-4.0E-03	0.03
d10	9.376	9.295	-8.1E-02	0.86
d11	12.762	12.734	-2.8E-02	0.22
d12	13.139	13.234	9.5E-02	0.72

d13	12.303	12.467	1.6E-01	1.34
d14	11.409	11.498	8.9E-02	0.78
d15	12.001	12.035	3.4E-02	0.28
d16	12.026	12.206	1.8E-01	1.49
d17	12.549	12.594	4.5E-02	0.36
d18	11.985	11.902	-8.3E-02	0.69
e1	9.664	9.539	-1.3E-01	1.30
e2	9.852	9.813	-3.8E-02	0.39
e3	10.640	10.549	-9.0E-02	0.85
e4	10.939	10.762	-1.8E-01	1.61
e5	10.765	10.736	-3.0E-02	0.28
e6	10.640	10.675	3.6E-02	0.34
e7	11.685	12.042	3.6E-01	3.05
e8	11.890	11.979	9.0E-02	0.75
e9	11.357	11.248	-1.1E-01	0.97
e10	11.425	11.320	-1.1E-01	0.92
e11	11.429	11.316	-1.1E-01	0.99
e12	10.674	10.771	9.7E-02	0.90
e13	10.390	10.229	-1.6E-01	1.55
e14	10.698	10.732	3.4E-02	0.32
e15	11.239	11.087	-1.5E-01	1.36
e16	11.045	11.189	1.4E-01	1.30
e17	10.558	10.681	1.2E-01	1.17
e18	10.471	10.440	-3.1E-02	0.30
e19	11.226	11.332	1.1E-01	0.94
e20	11.478	11.474	-4.5E-03	0.04
e21	10.441	10.751	3.1E-01	2.97
e22	10.541	10.572	3.1E-02	0.29
e23	10.581	10.556	-2.4E-02	0.23
e24	10.159	9.997	-1.6E-01	1.59
f1	9.379	9.242	-1.4E-01	1.46
f2	9.472	9.407	-6.6E-02	0.69
f3	9.550	9.626	7.6E-02	0.79
f4	9.567	9.513	-5.4E-02	0.56
f5	9.513	9.343	-1.7E-01	1.79

f6	9.786	9.651	-1.3E-01	1.38
f7	10.093	10.007	-8.6E-02	0.85
f8	10.412	10.427	1.5E-02	0.14
f9	10.444	10.245	-2.0E-01	1.91
f10	9.451	9.585	1.3E-01	1.41
f11	9.559	9.515	-4.4E-02	0.46
f12	9.371	9.344	-2.7E-02	0.29
f13	9.061	9.122	6.1E-02	0.67
f14	9.840	9.839	-7.8E-04	0.01
f15	9.702	9.715	1.3E-02	0.13
f16	9.588	9.607	2.0E-02	0.21
f17	9.646	9.715	6.9E-02	0.72
f18	9.857	9.845	-1.2E-02	0.12
f19	9.666	9.704	3.8E-02	0.39
f20	8.950	9.228	2.8E-01	3.10
f21	9.012	9.245	2.3E-01	2.58
f22	9.472	9.560	8.7E-02	0.92
f23	9.819	9.978	1.6E-01	1.62
f24	9.724	9.992	2.7E-01	2.76
f25	9.259	9.291	3.2E-02	0.34
f26	9.247	9.087	-1.6E-01	1.73
f27	8.996	8.999	3.1E-03	0.03
f28	8.778	8.616	-1.6E-01	1.85
f29	8.759	8.795	3.6E-02	0.41
f30	9.164	9.081	-8.3E-02	0.91
g5	9.103	9.072	-3.1E-02	0.34
g22	8.210	8.280	7.0E-02	0.85

Appendix C

The power per element comparison over all trials

element	abs max difference per element	Max difference (%)	average difference per element	Average difference (%)
b2	0.235	1.672	-0.012 ± 0.086	0.5 ± 0.4
b3	0.319	2.114	0.122 ± 0.09	0.8 ± 0.6
b4	0.352	2.421	0.205 ± 0.108	1.5 ± 0.6
b5	0.271	1.840	-0.016 ± 0.133	0.6 ± 0.6
b6	0.275	2.178	-0.008 ± 0.099	0.6 ± 0.5
c1	0.287	2.363	-0.068 ± 0.093	0.8 ± 0.5
c2	0.240	1.804	-0.021 ± 0.114	0.7 ± 0.6
c3	0.467	2.955	-0.254 ± 0.102	1.7 ± 0.7
c5	0.471	3.017	-0.206 ± 0.126	1.4 ± 0.7
c6	0.189	1.381	0.014 ± 0.107	0.6 ± 0.4
c7	0.298	2.014	0.015 ± 0.119	0.5 ± 0.5
c8	0.250	1.668	0.057 ± 0.139	0.8 ± 0.6
c9	0.238	1.606	0.023 ± 0.094	0.6 ± 0.4
c10	0.231	4.538	-0.018 ± 0.12	1.1 ± 1.0
c11	0.259	2.049	0.053 ± 0.106	0.7 ± 0.5
c12	0.176	1.289	0.034 ± 0.087	0.6 ± 0.3
d1	0.185	2.393	0.035 ± 0.08	0.9 ± 0.6
d2	0.277	2.365	0.055 ± 0.117	0.8 ± 0.7
d3	0.187	1.451	0.009 ± 0.088	0.5 ± 0.4
d4	0.293	2.465	0.031 ± 0.107	0.7 ± 0.6
d5	0.211	1.728	0.07 ± 0.091	0.7 ± 0.5
d6	0.260	1.913	0.069 ± 0.109	0.7 ± 0.6
d7	0.246	1.925	0.053 ± 0.112	0.8 ± 0.6
d8	0.333	2.395	-0.092 ± 0.108	0.8 ± 0.6
d9	0.199	1.891	-0.028 ± 0.086	0.6 ± 0.5
d10	0.210	2.382	-0.067 ± 0.076	0.8 ± 0.6
d11	0.252	2.161	0 ± 0.088	0.5 ± 0.5
d12	0.291	2.068	0.005 ± 0.143	0.8 ± 0.6
d13	0.357	2.840	0.041 ± 0.117	0.7 ± 0.7
d14	0.261	2.338	0.027 ± 0.11	0.8 ± 0.6
d15	0.210	1.801	-0.051 ± 0.097	0.8 ± 0.5

d16	0.305	2.275	-0.039 ± 0.11	0.7 ± 0.6
d17	0.243	1.973	0.017 ± 0.126	0.8 ± 0.6
d18	0.327	2.690	-0.055 ± 0.104	0.8 ± 0.6
e1	0.245	2.322	-0.085 ± 0.096	1.1 ± 0.7
e2	0.302	3.134	0.116 ± 0.097	1.3 ± 0.9
e3	0.216	1.990	-0.027 ± 0.099	0.8 ± 0.6
e4	0.303	2.951	-0.049 ± 0.114	0.9 ± 0.7
e5	0.237	2.341	0.061 ± 0.086	0.7 ± 0.7
e6	0.404	3.855	0.103 ± 0.118	1.1 ± 0.9
e7	0.672	5.628	0.397 ± 0.119	3.4 ± 1.0
e8	0.317	2.593	0.123 ± 0.126	1.3 ± 0.7
e9	0.265	2.372	-0.075 ± 0.125	1.0 ± 0.8
e10	0.305	2.557	-0.059 ± 0.105	0.7 ± 0.6
e11	0.199	1.988	-0.031 ± 0.12	0.9 ± 0.6
e12	0.309	2.999	0.063 ± 0.113	1.0 ± 0.7
e13	0.351	3.210	-0.119 ± 0.095	1.2 ± 0.9
e14	0.178	1.668	-0.028 ± 0.087	0.7 ± 0.5
e15	0.279	2.348	-0.037 ± 0.093	0.6 ± 0.6
e16	0.302	2.700	-0.059 ± 0.103	0.9 ± 0.7
e17	0.238	2.171	-0.071 ± 0.096	1.0 ± 0.6
e18	0.393	3.773	-0.163 ± 0.114	1.5 ± 1.0
e19	0.272	2.455	0.002 ± 0.125	0.8 ± 0.6
e20	0.405	3.582	-0.138 ± 0.111	1.2 ± 0.9
e21	0.310	2.971	0.054 ± 0.122	1.0 ± 0.7
e22	0.230	2.167	0.034 ± 0.079	0.6 ± 0.5
e23	0.175	1.641	0.036 ± 0.079	0.7 ± 0.5
e24	0.305	3.204	-0.093 ± 0.073	1.0 ± 0.8
f1	0.239	2.689	0.026 ± 0.11	1.0 ± 0.6
f2	0.252	2.533	0.035 ± 0.101	0.9 ± 0.7
f3	0.227	2.539	0.059 ± 0.111	1.1 ± 0.8
f4	0.190	2.084	0.048 ± 0.079	0.8 ± 0.5
f5	0.293	3.307	0.011 ± 0.108	0.9 ± 0.7
f6	0.243	2.382	0.056 ± 0.106	1.0 ± 0.6
f7	0.265	2.594	-0.058 ± 0.099	0.9 ± 0.7
f8	0.269	2.378	-0.01 ± 0.111	0.8 ± 0.7
f9	0.316	3.032	-0.166 ± 0.085	1.6 ± 0.7

f10	0.401	4.227	0.131 ± 0.09	1.4 ± 1.0
f11	0.253	2.601	0.067 ± 0.095	0.8 ± 0.8
f12	0.342	3.605	0.108 ± 0.122	1.5 ± 0.9
f13	0.394	4.365	0.16 ± 0.105	1.8 ± 1.1
f14	0.150	1.577	-0.015 ± 0.083	0.7 ± 0.5
f15	0.324	3.013	-0.067 ± 0.095	0.9 ± 0.7
f16	0.301	2.961	-0.064 ± 0.1	0.9 ± 0.8
f17	0.352	3.598	-0.006 ± 0.107	0.8 ± 0.8
f18	0.293	2.840	-0.018 ± 0.101	0.8 ± 0.7
f19	0.193	1.977	-0.004 ± 0.084	0.6 ± 0.5
f20	0.290	3.153	0.107 ± 0.09	1.2 ± 0.9
f21	0.245	2.651	0.093 ± 0.093	1.2 ± 0.8
f22	0.201	2.337	-0.02 ± 0.099	0.8 ± 0.6
f23	0.259	2.525	0.036 ± 0.139	1.3 ± 0.7
f24	0.402	4.615	0.17 ± 0.115	1.8 ± 1.2
f25	0.169	1.778	-0.073 ± 0.071	1.0 ± 0.4
f26	0.232	2.389	-0.127 ± 0.071	1.4 ± 0.7
f27	0.221	2.282	-0.061 ± 0.07	0.7 ± 0.7
f28	0.233	2.744	-0.099 ± 0.087	1.4 ± 0.7
f29	0.196	2.248	0.004 ± 0.11	1.1 ± 0.6
f30	0.276	3.074	0.023 ± 0.1	0.9 ± 0.7
g5	0.272	3.090	-0.007 ± 0.106	0.9 ± 0.8
g22	0.260	3.128	-0.007 ± 0.112	1.1 ± 0.9
max			0.397	3.4
min			-0.254	0.5
average			0.003 ± 0.009	1 ± 0.4